

# Intercalating Anions between Terminated Anion Layers: Unusual Ionic S–Se Bonds and Hole-Doping Induced Superconductivity in $S_{0.24}(NH_3)_{0.26}Fe_2Se_2$

Ruijin Sun,<sup>†,‡</sup> Shifeng Jin,<sup>\*,†,‡,§</sup> Lin Gu,<sup>†,‡,§</sup> Qinghua Zhang,<sup>†,‡</sup> Qingzhen Huang,<sup>||</sup> Tianping Ying,<sup>§</sup> YiRan Peng,<sup>⊥</sup> Jun Deng,<sup>†,‡</sup> Zhiping Yin,<sup>⊥</sup> and Xiaolong Chen<sup>\*,†,‡,§,||,∇</sup>

<sup>†</sup>Institute of Physics, Chinese Academy of Science, Beijing 100190, China

<sup>‡</sup>School of Physical Sciences, University of Chinese Academy of Sciences, Beijing 100190, China

<sup>§</sup>Department of Physics, Fudan University, Shanghai 200433, China

<sup>||</sup>NIST Center for Neutron Research, National Institute of Standards and Technology, Gaithersburg, Maryland 20899, United States

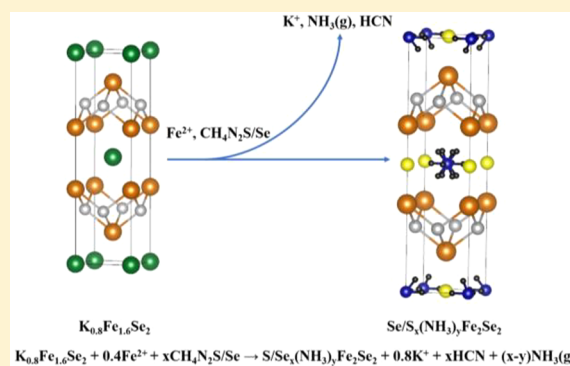
<sup>⊥</sup>Department of Physics and Center for Advanced Quantum Studies, Beijing Normal University, Beijing 100875, China

<sup>#</sup>Collaborative Innovation Center of Quantum Matter, Beijing 100190, China

<sup>∇</sup>Songshan Lake Materials Laboratory, Dongguan 523808, China

## Supporting Information

**ABSTRACT:** The pairing of ions of opposite charge is a central principle of chemistry. Even though the ability to intercalate anions is desirable for many applications, it remains a key challenge for numerous host materials with their outmost layers being anions. In this work, we introduce a hydrothermal ion-exchange synthesis to intercalate oxidative S and Se anions between the Se layers of FeSe, which leads to single crystals of novel compounds  $(Se/S)_x(NH_3)_yFe_2Se_2$ . In particular, the unusual anion–anion bonding between the intercalated S (or Se) and Se layers exhibits strong ionic characteristics. The charge transfer through the Se layer to S (or Se) intercalants is further confirmed by the elevated oxidation state of Fe ions and the dominant hole carriers in the intercalated compounds. By intercalating S, for the first time superconductivity emerged in hole-doped iron chalcogenides. The generality of this chemical approach was further demonstrated with layered FeS and NiSe. Our findings thus open an avenue to exploring diverse aspects of anionic intercalation in similar materials.



## INTRODUCTION

Intercalation, which enables the insertion of a charged or neutral species into a host lattice,<sup>1</sup> has sparked great interest for its wide-ranging applications in electrochemical energy storage,<sup>2–4</sup> electrochromic materials,<sup>5</sup> transparent conductive films,<sup>6</sup> and inducing unconventional or topological superconductivity.<sup>7</sup> In such cases, redox intercalation of charged species with host–guest charge transfer is crucial for tailoring the charge accumulation and properties of the host materials.<sup>8</sup> For intercalation of charged species, the main category defining the possible reactions is the charge on the host lattice. It is well established that in host materials carrying charges, such as the layered double hydroxides, the charge of the intercalants must stay opposite to maintain charge neutrality.<sup>9</sup> While for neutral host materials such as graphite and layered metal chalcogenides, both cations and anions should be available for intercalation through a reduction or oxidation reaction, making the application of such materials even more diverse.<sup>1</sup> However, to date, only graphite<sup>8</sup> and hexagonal-BN<sup>10</sup> have been shown

to be susceptible to intercalations of either cations or anions. For a majority of neutral host materials, such as layered metal chalcogenides (e.g., FeSe),<sup>11</sup> metal nitride halides (e.g., ZrNCl),<sup>12</sup> metal oxychlorides (e.g., FeOCl),<sup>13</sup> and metal phosphorus trichalcogenides (e.g., FePS<sub>3</sub>),<sup>14</sup> a key structural feature continues to prevent the intercalation of negatively charged species. In such materials, the metal layers are fully encapsulated by negatively charged nonmetal layers, which facilitates the intercalation of cations by forming ionic bonds with the outermost anion layers but still renders the intercalation of anions infeasible.<sup>15</sup> To enable anion intercalation in these materials, the resulting compounds should be stabilized by the rare anion–anion bonding. Thus, the procedure for inserting oxidative anions between adjacent anion layers remains a key synthesis challenge in intercalation chemistry, the solution of which may have broad implications

Received: June 3, 2019

Published: July 29, 2019

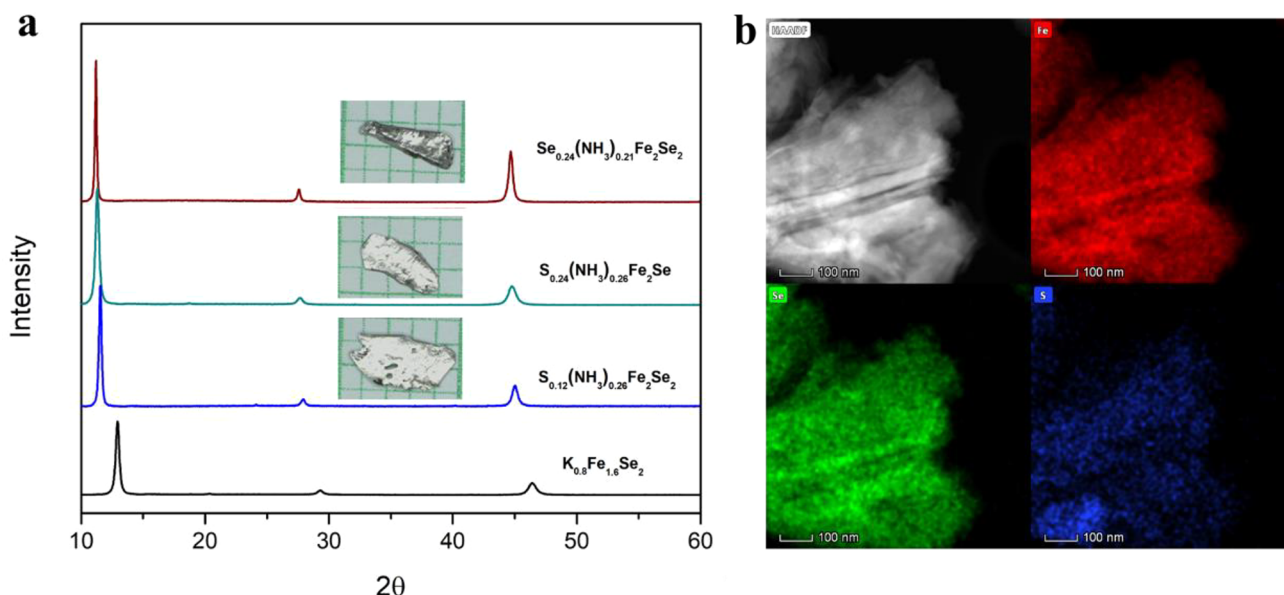


**Figure 1.** (a) Powder X-ray diffraction patterns along (00l) direction for  $\text{Se}/\text{S}_x(\text{NH}_3)_y\text{Fe}_2\text{Se}_2$  and  $\text{K}_{0.8}\text{Fe}_{1.6}\text{Se}_2$  single crystals. (b) HAADF image and compositional mapping of  $\text{S}_{0.12}(\text{NH}_3)_{0.26}\text{Fe}_2\text{Se}_2$ .

for anion intercalation and tailoring the properties of a large number of materials.

FeSe is a prominent member of the well-known family of iron–chalcogenide superconductors.<sup>11</sup> Like other layered chalcogenides, such as transition-metal dichalcogenides (TMDs), the metal layer of FeSe is encapsulated by chalcogenide layers, and the adjacent chalcogenide layers are combined together as a bulk solid by van der Waals interactions.<sup>16</sup> Since the heterovalence substitution in FeSe easily destroys its superconductivity,<sup>17</sup> the carrier doping in FeSe, which is crucial for enhancing its unconventional superconductivity, relies on the host–guest charge transfer caused by redox intercalation.<sup>18</sup> By inserting reductive K, we have shown that electron-doping and enhanced superconductivity can be achieved in FeSe by intercalating cations.<sup>19</sup> Subsequently, a large number of metal cations such as alkali metals,<sup>20,21</sup> alkaline earth metals, and rare earth metals<sup>22</sup> as well as a range of neutral or positively charged molecules, including  $\text{NH}_3$ ,<sup>23</sup> cetyltrimethylammonium ( $\text{CTA}^+$ ),<sup>24</sup>  $\text{LiOH}$ ,<sup>25</sup> and other organic molecules,<sup>26,27</sup> were generally introduced into the iron–chalcogenide system to form a large electron-doped superconducting family. The exotic electronic structure without hole-carriers<sup>28</sup> and the recently discovered Majorana quasiparticles<sup>29</sup> in this system are hotly debated in the field of superconductivity. Despite recent advances in electron-doped iron selenides, hole-doping in FeSe has not been achieved yet, which is highly desirable for understanding the superconducting mechanism and exploring potential applications. The absence of hole-doped FeSe-based superconductors is mainly due to the aforementioned difficulties in intercalating anions between anionic chalcogen layers.

Herein, we report a general chemical strategy for intercalating oxidizing S and Se anions between chalcogen layers in FeSe and related layered chalcogenides. In particular, hole-doping-induced enhanced superconductivity is first realized in a FeSe-based compound,  $\text{S}_{0.24}(\text{NH}_3)_{0.26}\text{Fe}_2\text{Se}_2$ , in the form of large single crystal up to 0.8 cm. The crystal structures determined by single crystal and neutron powder diffraction data revealed that the intercalated S (or Se) anions

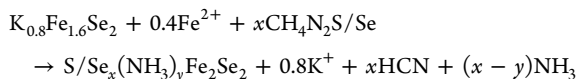
are coordinated by two Se anions of the adjacent Se layers. In particular, the charge density analysis based on the state-of-art DFT-DMFT calculations shows strong ionic characteristics in the unusual S–Se and Se–Se bonds, accompanied by the significantly enlarged hole pockets after intercalation, suggesting that charge transfer occurred between the Se layer and S (or Se) intercalants. The findings are supported by the enhanced oxidation state of Fe ions probed by both X-ray photoelectron and  $^{57}\text{Fe}$  Mössbauer spectra as well as the dominant hole-carriers in the intercalated compounds as revealed by Hall resistivity measurements. As a result of tuning the content of Se and S, enhanced superconductivity emerged from a nonsuperconducting strange metal. The generality of this anion intercalation chemical approach was further demonstrated with other layered chalcogenides, that is, FeS and NiSe. The findings reported here not only open an avenue to the exploration and investigation of hole-doped iron chalcogenide superconductors but may also have broader implications for a large number of similar materials that have exhibited resistance to anion intercalation.

## RESULTS AND DISCUSSION

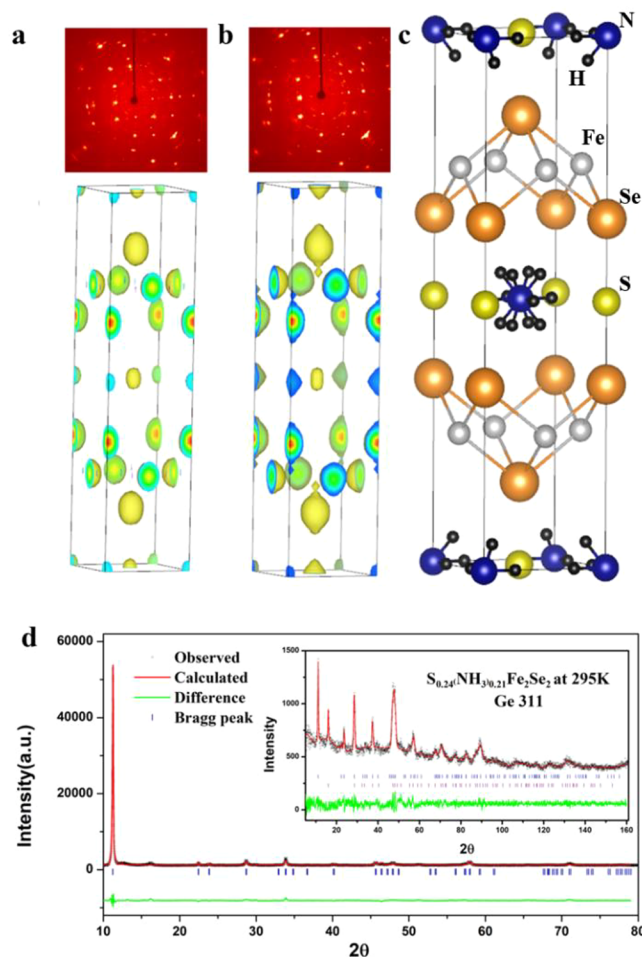
**Synthetic Procedures and Characterizations of  $(\text{Se}/\text{S})_x(\text{NH}_3)_y\text{Fe}_2\text{Se}_2$ .** The sulfur- or selenium-intercalated compounds were synthesized using the  $\text{K}_{0.8}\text{Fe}_{1.6}\text{Se}_2$  single crystal as the precursor (the procedure is detailed in the [Experimental Section](#)). Thiourea and selenourea were used as mild oxidants that easily decompose and release S and Se ions in hot water. Thiourea (alfa, 99.9% purity) or selenourea (alfa, 99.9% purity) was dissolved in 10 mL of deionized water in a Teflon-lined stainless-steel autoclave (volume 25 mL). Nano crystalline iron powder (Aladdin Industrial, ~50 nm in size, 99.99% purity) and pieces of  $\text{K}_{0.8}\text{Fe}_{1.6}\text{Se}_2$  crystals were added to the solution. Finally, the autoclave was sealed and heated at 100–130 °C for 80 h. The composition of the sulfur-intercalated compounds can be adjusted by tuning the concentration of thiourea, which yields two S intercalated samples I and II, whereas the replacement of thiourea with selenourea yield another Se-intercalated sample III (detailed in

Table S1). After the reactions, large single crystals up to 0.8 cm with silver metallic luster were obtained by leaching and clearing (Figure 1a). Powder X-ray diffractions show that the (00l) reflections of the  $K_{0.8}Fe_{1.6}Se_2$  precursor are completely replaced by a new set after reactions; see Figure 1a. The lowest angle Bragg peaks at  $d$ -spacing of  $\sim 7.6$ – $7.9$  Å,  $\sim 10\%$  larger than that for  $K_{0.8}Fe_{1.6}Se_2$ , suggest that new species are intercalated between the FeSe layers. We further exfoliated the crystals of samples I using Scotch tape, which resulted in samples thin enough to obtain the high-angle-annular-dark field (HAADF) images (Figure 1b). As shown in Figure 1b, the elemental mapping shows a homogeneous distribution of Fe, Se, and S atoms after the intercalation reactions.

Several different characterization techniques were used to determine the elemental composition of the three new compounds. As shown in Figure S1 and Tables S2–S4, inductively coupled plasma atomic emission spectroscopy (ICP-AES) and energy-dispersive X-ray spectroscopy (EDX) measurements indicate that all products contain no residual K. The atomic ratio of Fe/Se is close to 1:1 for the two S intercalated samples (I and II), suggesting that the FeSe layers remain intact after the reactions, and the maximum S/Se ratio reached 12 atom % in sample II. For the Se-intercalated sample (III), the atomic ratio of Se/Fe increased considerably to 52.83/47.17, and the excess Se/Fe ratio reached 12 atom % as well. Further, TG-DTA thermogravimetric data (Figure S2) for all of the samples indicate notable weight losses during heating. The chemical analysis of released species using a CHN elemental analyzer indicated an N/H/C atomic ratio of 0.32(1):1:0, suggesting that the  $NH_3$  molecule was cointercalated along with sulfur/selenium. According to the results presented in Tables S2–S4, the chemical formulas of the three intercalation compounds are determined to be  $S_{0.12}(NH_3)_{0.26}Fe_2Se_2$  (I),  $S_{0.24}(NH_3)_{0.26}Fe_2Se_2$  (II), and  $Se_{0.24}(NH_3)_{0.21}Fe_2Se_2$  (III), respectively. Based on the determined compositions, the reaction pathway for the new phases  $Se/S_x(NH_3)_yFe_2Se_2$  can be described as follows:



**Crystal Structure of  $(Se/S)_x(NH_3)_yFe_2Se_2$ .** To determine the crystal structures of the intercalation compounds, two small specimens of  $S_{0.12}(NH_3)_{0.26}Fe_2Se_2$  ( $152 \times 66 \times 11 \mu m^3$ ) and  $Se_{0.24}(NH_3)_{0.21}Fe_2Se_2$  ( $73 \times 41 \times 12 \mu m^3$ ) were selected for the single-crystal X-ray analysis. Parts a and b of Figure 2 display the diffraction patterns for the two samples. The initial crystal structures of  $S_{0.12}(NH_3)_{0.26}Fe_2Se_2$  and  $Se_{0.24}(NH_3)_{0.21}Fe_2Se_2$  were determined with lattice parameters  $a = 3.8528(2)$  Å,  $c = 15.2330(3)$  Å and  $a = 3.8605(2)$  Å,  $c = 15.8008(3)$  Å, respectively. Both exhibit a tetragonal structure with space group  $I4/mmm$ . The electron density maps shown in Figure 2a,b were constructed using the charge flipping method implemented in Jana2006.<sup>30</sup> The positions of intercalated S/Se anions and  $NH_3$  molecules can be clearly located at either the 2a site ( $1/2, 1/2, 1/2$ ) or the 2b site ( $0, 0, 1/2$ ). In particular, we note that the charge density for the Se-intercalated sample increases considerably in the 2b site, suggesting that S or Se was located at the 2b site ( $0, 0, 1/2$ ). Based on this model, the structure refinements rapidly converged to small residuals ( $R1 = 0.027$  for I and 0.053 for III). The crystallographic parameters are compiled in Tables S7 and S9 in the Supporting Information.



**Figure 2.** SCXRD patterns and charge density distribution from SCXRD for (a)  $S_{0.12}(NH_3)_{0.26}Fe_2Se_2$  and (b)  $Se_{0.24}(NH_3)_{0.21}Fe_2Se_2$ . (c) Structure model for  $Se/S_x(NH_3)_yFe_2Se_2$ . (d) Observed (black crosses) and calculated (solid red line) PXRD and NPD pattern (inset) for  $S_{0.24}(NH_3)_{0.26}Fe_2Se_2$  at 295 K. Allowed peak positions are marked by vertical lines: from the top, the main phase (blue) and minor phases (purple)—FeSe.

The final crystal structure of  $S_{0.24}(NH_3)_{0.26}Fe_2Se_2$ , including the position of H atoms, was completed by neutron powder diffraction (NPD) data (see the Experimental Section). As shown in the inset of Figure 2d, the constituent H produced a characteristic incoherent background in the NPD pattern. A structural model based on space group  $I4/mmm$  was adopted following the results of single-crystal X-ray refinements, and the remaining nuclear scattering density is revealed by computing Fourier difference maps. The refinement resulted in a satisfactory fit to the NPD data, with the H atoms located on the 16m site ( $x, x, z$ ), bonded to the N atom (2a site ( $0, 0, 0$ )) at about 1 Å. S was located at site ( $0, 0, 1/2$ ) (2b site) between the two Se anions in layers. Refinement of the site occupancies of the  $NH_3$  and the S leads to a composition of  $S_{0.24(1)}(NH_3)_{0.26(1)}Fe_2Se_2$ , which is consistent with the sample composition by chemical analysis. The tables of refined parameters are deposited in Table S8, and this structural model is further confirmed by the Rietveld refinement against powder X-ray data shown in Figure 2d.

To probe the effect of S or Se intercalations on the crystal structures, we turned our attention to the geometry of  $FeSe_4$  tetrahedra because of their sensitivity to carrier doping. It is

widely acknowledged that the  $\text{FeSe}_4$  tetrahedra are compressed in pristine  $\text{FeSe}$  and that upon electron-doping the  $\text{FeSe}_4$  tetrahedra are distorted further. As shown in Table S5, the geometry of  $\text{FeSe}_4$  tetrahedra responds in an opposite way in samples I–III. For instance, the Se–Fe–Se bond angles are  $107.664(3)^\circ$  ( $\times 2$ ) and  $110.800(4)^\circ$  ( $\times 4$ ) in  $\text{S}_{0.24(1)}(\text{NH}_3)_{0.26(1)}\text{Fe}_2\text{Se}_2$ , in comparison with  $103.9^\circ$  ( $\times 2$ ) and  $112.3^\circ$  ( $\times 4$ ) for  $\text{FeSe}$  and  $102.9^\circ$  ( $\times 2$ ) and  $112.8^\circ$  ( $\times 4$ ) for electron-doped  $\text{Li}_{0.6}(\text{ND}_2)_{0.2}(\text{ND}_3)_{0.8}\text{Fe}_2\text{Se}_2$ .<sup>20</sup> Moreover, the bond length of  $\text{FeSe}$  in samples I–III is close to or even smaller than that of pristine  $\text{FeSe}$ , which is also opposite to the effect of electron doping, which trends to elongate the  $\text{FeSe}$  bonds. In short, the structural evolution of the  $\text{FeSe}$  layer upon S/Se intercalations systematically deviates from the known effect of electron doping.

**Host–Guest Charge Transfer in  $(\text{Se}/\text{S})_x(\text{NH}_3)_y\text{Fe}_2\text{Se}_2$ .** X-ray photoelectron spectroscopy (XPS) is a powerful technique for investigating the charge transfer and valence state of materials. Figure 3a–c and Figure S3 present the XPS

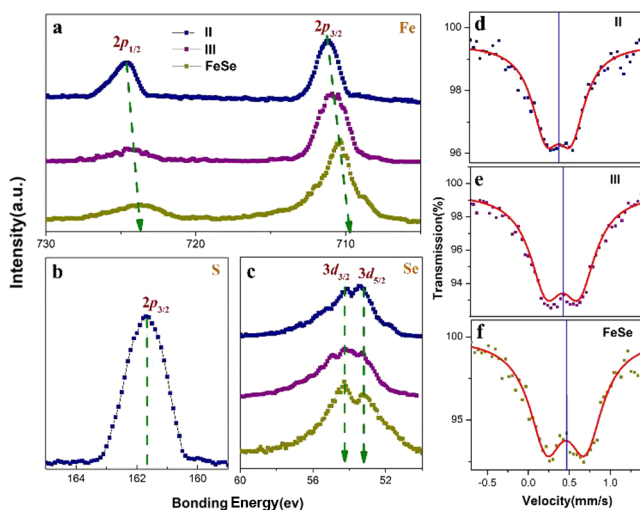


**Figure 3.** (a–c) XPS pattern of  $\text{S}_{0.24}(\text{NH}_3)_{0.26}\text{Fe}_2\text{Se}_2$ (II),  $\text{Se}_{0.24}(\text{NH}_3)_{0.21}\text{Fe}_2\text{Se}_2$ (III), and  $\text{FeSe}$  at 300 K. (d–f)  $^{57}\text{Fe}$  Mössbauer spectra of (d)  $\text{S}_{0.24}(\text{NH}_3)_{0.26}\text{Fe}_2\text{Se}_2$ , (e)  $\text{Se}_{0.24}(\text{NH}_3)_{0.21}\text{Fe}_2\text{Se}_2$ , and (f)  $\text{FeSe}$  at 300 K. The zero-velocity origin is relative to  $\alpha\text{-Fe}$  at room temperature.

pattern of Fe 2p, Se 3d, S 2p, and N 1s core-level spectra of  $\text{S}_{0.24}(\text{NH}_3)_{0.26}\text{Fe}_2\text{Se}_2$ ,  $\text{Se}_{0.24}(\text{NH}_3)_{0.21}\text{Fe}_2\text{Se}_2$ , and pristine  $\text{FeSe}$  measured at 300 K. Upon S intercalation, the binding energy of Fe 2p<sub>3/2</sub> (711.15 eV) increased by 0.25 eV in comparison with the value in  $\text{FeSe}$  (710.9 eV)<sup>31</sup> but was still 0.65 eV smaller than the binding energy in  $\text{FeCl}_3$  (711.8 eV).<sup>32</sup> Notably, the measured binding energy for S 2p<sub>3/2</sub> is 161.9 eV, the same as in  $\text{CdS}$  (161.9 eV)<sup>33</sup> and far from the value in the S element (164.0 eV).<sup>34</sup> The binding energy of N 1s (399.8 eV) is very close to that of ammonia intercalated compounds,<sup>35</sup> confirming that nitrogen exists in the form of neutral ammonia molecules (Figure S3). The XPS results indicate the  $\text{Fe}^{2+}$  ions are partially oxidized, suggesting the hole-carriers are transferred into  $\text{FeSe}$  layers. Therefore, the charge balance formula of  $\text{S}_{0.24}(\text{NH}_3)_{0.26}\text{Fe}_2\text{Se}_2$  can be written as  $[(\text{S})^{2-}]_{0.24}[\text{NH}_3]_{0.26}[(\text{Fe})^{2.24+}]_2[(\text{Se}^{2-})]_2$ . Similarly, for the Se-intercalated samples, the binding energy of Fe 2p<sub>3/2</sub> (711.08 eV) increases by 0.18 eV, indicating that the iron is also oxidized upon Se intercalation, but to a less extent,

possibly due to the lower electronegativity of Se in comparison with S.

Because the XPS technique is more surface sensitive, we further characterized the valence state of Fe in  $(\text{Se}/\text{S})_x(\text{NH}_3)_y\text{Fe}_2\text{Se}_2$  using  $^{57}\text{Fe}$  Mössbauer spectra, which is an inherent bulk technique. For nonmagnetic materials, the Fe valence state can be probed by both isomer shift and quadrupole-splitting parameters. In the case of  $\text{FeSe}$  and its intercalation compounds, the coordination number of Fe is unchanged, which means that an increase in the Fe valence state should decrease both the isomer shift and quadrupole splitting parameters. As shown in Figure 3d–f, the isomer shifts of  $\text{FeSe}$ ,  $\text{Se}_{0.24}(\text{NH}_3)_{0.21}\text{Fe}_2\text{Se}_2$ , and  $\text{S}_{0.24}(\text{NH}_3)_{0.26}\text{Fe}_2\text{Se}_2$  are determined to be 0.46(2), 0.43(4), and 0.37(2) mm/s, respectively. The quadrupole splitting parameters of  $\text{FeSe}$ ,  $\text{Se}_{0.24}(\text{NH}_3)_{0.21}\text{Fe}_2\text{Se}_2$ , and  $\text{S}_{0.24}(\text{NH}_3)_{0.26}\text{Fe}_2\text{Se}_2$  are determined to be 0.415(1), 0.325(2), and 0.249(1) mm/s, respectively. The decreases in isomer shift and quadrupole splitting parameters consistently suggest that the valence of Fe is increased by intercalating Se, and to a larger extent by intercalating S, which is in line with the XPS data and further confirmed hole-carriers doping in  $\text{Se}/\text{S}_x(\text{NH}_3)_y\text{Fe}_2\text{Se}_2$  serial compounds.

**Analysis of the Bonding and Electronic Structure.** The finding that S/Se intercalants oxidized the  $\text{FeSe}$  layer in  $\text{Se}/\text{S}_x(\text{NH}_3)_y\text{Fe}_2\text{Se}_2$  has an interesting consequence, which means the chemical bonds between S/Se intercalants and  $\text{FeSe}$  layers should have high ionic characteristics. This seems quite unusual, considering that S/Se intercalants actually bond with Se. To clarify the bonding nature between (S/Se)–Se and the consequence of S/Se intercalation, we performed ab initio DFT-DMFT calculations using the Win2K code to investigate the charge density and electronic structure. The charge density  $\rho(r)$ , Laplacian for charge density  $\nabla^2\rho(r)$ , and the algebraic sum of the three principal curvatures  $\lambda_1$ ,  $\lambda_2$  (perpendicular to the bond), and  $\lambda_3$  (parallel to the bond) of  $\rho(r)$  are the appropriate tools for analyzing the bonding nature based on charge density.<sup>36</sup> In Figure 4 and Table S6, we present the results of the topological analysis of the charge concentration and depletion at bond critical point (BCP, where  $\nabla\rho(r_{\text{BCP}}) = 0$ ) based on the state-of-art DFT-DMFT calculations. First, the charge density at the BCP of the Se–S/Se bonds is remarkably lower than those bonds classified as polar covalent bonds, including third-row elements such as S and P, and is closer to the ionic Zr–N bond.<sup>37</sup> Second, as a signature of ionic bond characteristics, the Laplacians at the BCPs for Se–S/Se bonds are both positive, with the  $\nabla^2\rho(r_{\text{BCP}})$  reaching 3.09 and 3.34 for Se–S and Se–Se bonds, respectively. Third, the ratios of  $|\lambda_1|/\lambda_3$  for Se–S and Se–Se bonds are 0.376 and 0.452, and a value smaller than 1 is a good indication of high ionic characteristics. In short, the topological analysis on the charge density consistently suggests that the bonding between the S/Se anions and  $\text{FeSe}$  layers have strong ionic characteristics.

The deformation charge densities,  $\rho_{\text{def}} = \rho_{\text{crystal}} - \rho_{\text{IAM}}$  (IAM = independent atom model), in the Fe–Se–S (or Se) planes of the two structures are shown in Figure 4c,d. These plots show the expected features of a polar covalent bond between Fe–Se, as revealed by the positive density peaks in the internuclear Fe–Se regions. Notably, no obvious charge accumulation exists in the internuclear Se–S or Se–Se region, in sharp contrast to the common covalent bonds between chalcogen atoms in other materials. The rare ionic characteristics of the Se/S–Se bond play a key role in oxidizing the  $\text{FeSe}$  layer

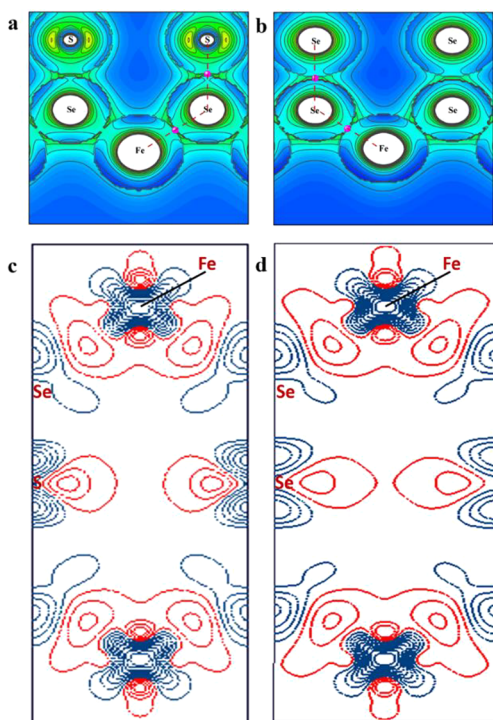


**Figure 4.** (a, b) Laplacian for charge density  $\rho(r)$  in the Se–Fe–S ( $S_{0.24}(\text{NH}_3)_{0.26}\text{Fe}_2\text{Se}_2$ ) plane and Se–Fe–Se ( $\text{Se}_{0.24}(\text{NH}_3)_{0.21}\text{Fe}_2\text{Se}_2$ ) plane. Positive values of  $\nabla^2\rho(r)$  are depicted by green and negative by blue. Red dash is the guiding line for the bond and purple dot is the critical point in the bond that  $\nabla\rho(r) = 0$ . The gray line is the contour line for the charge density. (c, d) Charge density difference for  $S_{0.24}(\text{NH}_3)_{0.26}\text{Fe}_2\text{Se}_2$  and  $\text{Se}_{0.24}(\text{NH}_3)_{0.21}\text{Fe}_2\text{Se}_2$  using the contour increment is 0.05 electron  $\times \text{Å}^{-3}$ . Positive contours are plotted with red lines. Negative contours are plotted with blue lines.

because the formation of Se/S–Se covalent bonds will weaken the oxidizability of Se within the FeSe layer and reduce the valence of Fe.

The amounts of charge transfer between the FeSe host layer and S/Se intercalants can also be derived from integrating the electron density over the atoms. According to Bader's analysis of the charge density, the pristine FeSe layers are generally charge compensating (Fe + 0.41 e, Se –0.41e). In contrast, in  $S_x(\text{NH}_3)_y\text{Fe}_2\text{Se}_2$ , a considerable number of electrons transferred from the FeSe host layer to S intercalants ((FeSe)<sub>2</sub>, + 0.28 e; S –0.28 e), in line with the previous experimental finding that FeSe is oxidized upon S intercalation. Moreover, a similar analysis of  $\text{Se}_x(\text{NH}_3)_y\text{Fe}_2\text{Se}_2$  suggests the host–guest electron transfer occurred to a lesser extent under Se intercalation ((FeSe)<sub>2</sub>, +0.10e; Se, –0.10e).

Parts a–c of Figure 5 show the band structures of  $S_{0.24}(\text{NH}_3)_{0.26}\text{Fe}_2\text{Se}_2$ ,  $\text{Se}_{0.24}(\text{NH}_3)_{0.21}\text{Fe}_2\text{Se}_2$ , and FeSe calculated using the DMFT-DFT method (Figure S6 presents the band structures calculated by DFT). For bulk FeSe, there are four bands crossing the Fermi level, with two hole-like bands around the zone center (M point) and two electron-like bands around the zone corner (Γ point). Luttinger's theorem states that the volume enclosed by a material's Fermi surface (FS) is directly proportional to the particle density. For bulk FeSe, the volumes enclosed by the Fermi surface are found to be 0.230 holes/cell and 0.231 electrons/cell, in line with the almost compensate electronic and hole carriers in bulk FeSe.<sup>38,39</sup> Because the S anion is intercalated into the FeSe layer, a new

hole-like pocket emerged at Γ point. Parts d and g of Figure 5 present the Fermi surface of  $S_{0.24}(\text{NH}_3)_{0.26}\text{Fe}_2\text{Se}_2$ . In comparison to bulk FeSe (Figure 5c), a new hole type FS occurred in  $S_{0.24}(\text{NH}_3)_{0.26}\text{Fe}_2\text{Se}_2$  at Γ point. Two types of Fermi surface coexisted in this system: two 2D cylinder-like FSs and a large-size 3D ellipsoid-like FS, analogous to hole-doped iron pnictide superconductors, e.g.,  $\text{Ba}_{0.67}\text{K}_{0.33}\text{Fe}_2\text{As}_2$ .<sup>40</sup> The volumes enclosed by the Fermi surface are found to be 0.925 holes/cell and 0.305 electrons/cell, namely a carrier density of  $4.02 \times 10^{21}$  holes/cm<sup>3</sup> and  $1.32 \times 10^{21}$  electrons/cm<sup>3</sup>. This result suggests that the S intercalation significantly increased the hole carrier concentration but decreased the electron-carrier concentration. Further calculation of  $\text{Se}_{0.24}(\text{NH}_3)_{0.21}\text{Fe}_2\text{Se}_2$  shows that the three hole-like pockets still existed around Γ point, and maintained a similar topology with  $S_{0.24}(\text{NH}_3)_{0.26}\text{Fe}_2\text{Se}_2$ . The enclosed hole carriers are 0.893 hole/cell, namely a carrier density of  $3.8 \times 10^{21}$  holes/cm<sup>3</sup>, roughly equal to  $S_{0.24}(\text{NH}_3)_{0.26}\text{Fe}_2\text{Se}_2$ . However, the enclosed electron carriers are slightly larger, that is, 0.412 electrons/cell, namely a carrier density of  $1.7 \times 10^{21}$  electron/cm<sup>3</sup>.

#### Dominant Hole-Carriers and Superconductivity.

Figure 6a,b and Figure S4 display the field (B) dependent Hall resistivity  $\rho_{xy}$  for  $S_{0.24}(\text{NH}_3)_{0.26}\text{Fe}_2\text{Se}_2$  and  $\text{Se}_{0.24}(\text{NH}_3)_{0.21}\text{Fe}_2\text{Se}_2$ . It is worth noting that in FeSe, the  $\rho_{xy}$  show a notable quadratic dependence on B, and the data are best fitted by a two-band model, with comparable contributions from both electron and hole carriers. In contrast, the measured Hall resistivity  $\rho_{xy}(B)$  of  $S_{0.24}(\text{NH}_3)_{0.26}\text{Fe}_2\text{Se}_2$  and  $\text{Se}_{0.24}(\text{NH}_3)_{0.21}\text{Fe}_2\text{Se}_2$  show a good linear dependence on B up to 9 T. This linear behavior of Hall resistivity is described by a single-band model, suggesting that the Fermi surface of the intercalated compounds is dominated by one type of carriers. More importantly, the derived Hall coefficients  $R_H = \rho_{xy}/\mu_0H$  is positive from 20 to 250 K, confirming that the dominant carriers in the two compounds are holes, in line with the XPS, and Mössbauer spectra results that indicate that the FeSe layers are oxidized (hole doped) after the intercalations. The carrier densities of  $S_{0.24}(\text{NH}_3)_{0.26}\text{Fe}_2\text{Se}_2$  and  $\text{Se}_{0.24}(\text{NH}_3)_{0.21}\text{Fe}_2\text{Se}_2$  fitted by a single-band model are listed in Table S10.

Figure 7a shows the temperature dependence of in-plane resistivity  $\rho_{ab}(T)$  at zero field from 10 to 200 K. For all the measured samples, the in-plane resistivity  $\rho_{ab}(T)$  exhibits a metallic behavior. Notably, the Se intercalated sample presents a linear variation of resistivity with temperature, a striking deviation from the conventional metallic (Fermi liquid) behavior. Upon S intercalation, the  $T^2$  dependent resistivity is gradually resumed by increasing the S contents. Moreover, sharp superconducting transitions appear for S intercalated  $S_x(\text{NH}_3)_y\text{Fe}_2\text{Se}_2$  samples, with the onset superconducting transition temperature  $T_c^{\text{onset}} = 7$  K at  $x = 0.12$  (I) and further enhanced to 11.5 K at  $x = 0.24$  (II). As shown in Figure 7b, the ZFC dc magnetic susceptibility  $4\pi\chi(T)$  of two  $S_x(\text{NH}_3)_y\text{Fe}_2\text{Se}_2$  crystals at  $\mu = 1$  mT shows consistently that the superconducting shielding emerges at 7 and 11 K, with a rather sharp transition width. The superconducting volume fractions (SVFs) estimated from the ZFC data are about 100%, indicating bulk superconductivity in hole doped  $S_x(\text{NH}_3)_y\text{Fe}_2\text{Se}_2$  single crystals. Furthermore, as shown in Figure S7, a clear jump in the specific heat ( $C_p$ ) is observed around the transition temperature  $T_c$ , and this signature of superconductivity is considerably suppressed under external magnetic field up to 5 T. We further fit the  $C_p(5T)$  data above  $T_c$  using the equation  $C_p/T = \gamma + \beta T^2$ , with fitted  $\gamma = 0.2842$

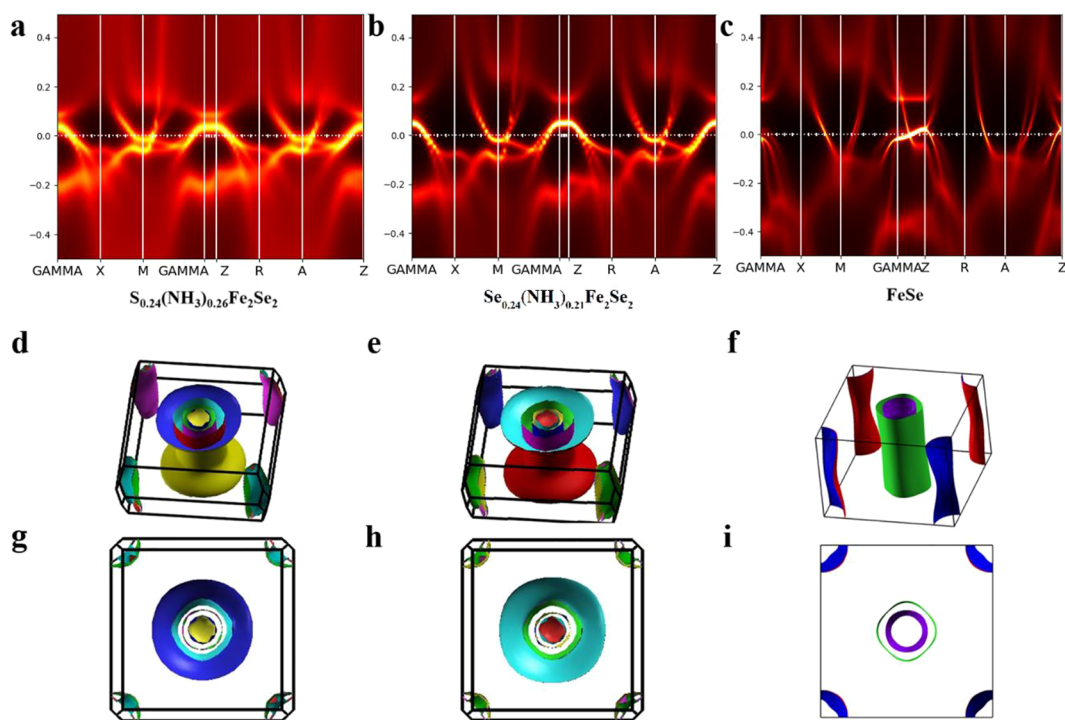


**Figure 5.** (a–c) The band structures calculated by the DFT-DMFT method of  $S_{0.24}(\text{NH}_3)_{0.26}\text{Fe}_2\text{Se}_2$ ,  $\text{Se}_{0.24}(\text{NH}_3)_{0.21}\text{Fe}_2\text{Se}_2$  and bulk FeSe. (d–f) Fermi surface of  $S_{0.24}(\text{NH}_3)_{0.26}\text{Fe}_2\text{Se}_2$ ,  $\text{Se}_{0.24}(\text{NH}_3)_{0.21}\text{Fe}_2\text{Se}_2$  and bulk FeSe ( $\Gamma$  point is at the center and M or X point is at the corner). (g–i) Vertical view of the Fermi surface. The Fermi energy is set to zero.

$\text{mJ g}^{-1} \text{K}^{-2}$ ,  $\beta = 0.00162 \text{ mJ g}^{-1} \text{K}^{-4}$ . Meanwhile, extrapolating the  $C_p(0T)$  data to 0 K leads to a residual  $\gamma_n = 0.0994 \text{ mJ g}^{-1} \text{K}^{-2}$ , the results indicating that the SVFs exceed 65%. The clear tendency between increased S contents and enhanced  $T_c$  suggest that the  $S_x(\text{NH}_3)_y\text{Fe}_2\text{Se}_2$  ( $x = 0.12, 0.24$ ) superconductors are still under-doped. To realize high temperature superconductivity in hole-doped FeSe systems, future effects are necessary to increase the contents of S, or researchers should try to introduce other stronger oxidant in between the FeSe layers.

It is worth noting that we have also succeeded in intercalating S or Se anions into other metal chalcogenides, such as NiSe and FeS, based on a similar ion-exchange method. The single crystals of metal cation intercalated  $\text{KNi}_2\text{Se}_2$  and  $\text{KFe}_{1-x}\text{S}_2$  are used instead as the precursors. In Figure S5, we present the as-synthesized S intercalated  $S_x(\text{NH}_3)_y\text{Ni}_2\text{Se}_2$  and  $S_x(\text{NH}_3)_y\text{Fe}_2\text{S}_2$  single crystals as well as their charge density based on single-crystal diffractions and powder diffraction data. The similarity of charge density between the two compounds and  $S_x(\text{NH}_3)_y\text{Fe}_2\text{Se}_2$  suggests that they are isostructural, and that S has been successfully intercalated between the NiSe and FeS layers. For many decades, only graphite and hexagonal-BN have been known to be susceptible to intercalations of either cations or anions. Our findings suggest that based on this ion-exchange strategy, even more layered solids that accommodate either cations or anions intercalants can be obtained and investigated in future research.

## CONCLUSION

We report a general chemical strategy for intercalating oxidizing chalcogenide anions into FeSe single crystals using a hydrothermal ion-exchange redox reaction. We successfully intercalated both S and Se anions along with  $\text{NH}_3$  molecules

into FeSe to form almost centimeter-sized single crystals of compounds:  $\text{Se}/S_x(\text{NH}_3)_y\text{Fe}_2\text{Se}_2$ . The determined crystal structures revealed direct anion–anion bonding between the chalcogenide intercalants and the FeSe layer. XPS,  $^{57}\text{Fe}$  Mössbauer spectra and Hall measurement consistently suggested that the S/Se intercalation involve hole-carrier doping, resulting in partial oxidation of the FeSe sheets. Quantitative analyses based on theoretical charge density demonstrated that the interlayer S–Se or Se–Se bonds have high ionic characteristics. As a result of the oxidizing anionic intercalation, the S intercalated compound represents the first example of hole-doped FeSe superconductors. Our results open up new possibilities for exploring hole-doped iron chalcogenide superconductors. Moreover, the synthesis strategy reported here may have broader implications for a large number of similar host materials that have exhibited resistance to anion intercalation.

## EXPERIMENTAL SECTION

**Sample Synthesis.** For the first step,  $\text{K}_{0.8}\text{Fe}_{1.6}\text{Se}_2$  crystals were grown using the self-flux method as a matrix, which yield pieces of  $\text{K}_{0.8}\text{Fe}_{1.6}\text{Se}_2$  crystals with golden metallic luster. Then, thiourea (Alfa, 99.9% purity) or selenourea (Alfa, 99.9% purity) was dissolved in 10 mL of deionized water in a Teflon-lined stainless steel autoclave (volume 25 mL). Nano crystalline iron powder (Aladdin Industrial, ~50 nm in size, 99.99% purity) and several pieces of  $\text{K}_{0.8}\text{Fe}_{1.6}\text{Se}_2$  crystals were added to the solution. Finally, the autoclave was sealed and heated to 100–130 °C for 80 h. Upon recovery, large single crystals with a different silver metallic luster were obtained by leaching and clearing. In the case of thiourea, two thiourea concentrations of 0.4–0.45 and >0.5 g/mL were used to tune the composition of intercalated S cations, which yielded samples I and II. In the case of selenourea, the highest quality sample was obtained at a selenourea concentration of 10%, which yield samples III. The nominal stoichiometry for each crystal is listed in Table S1.

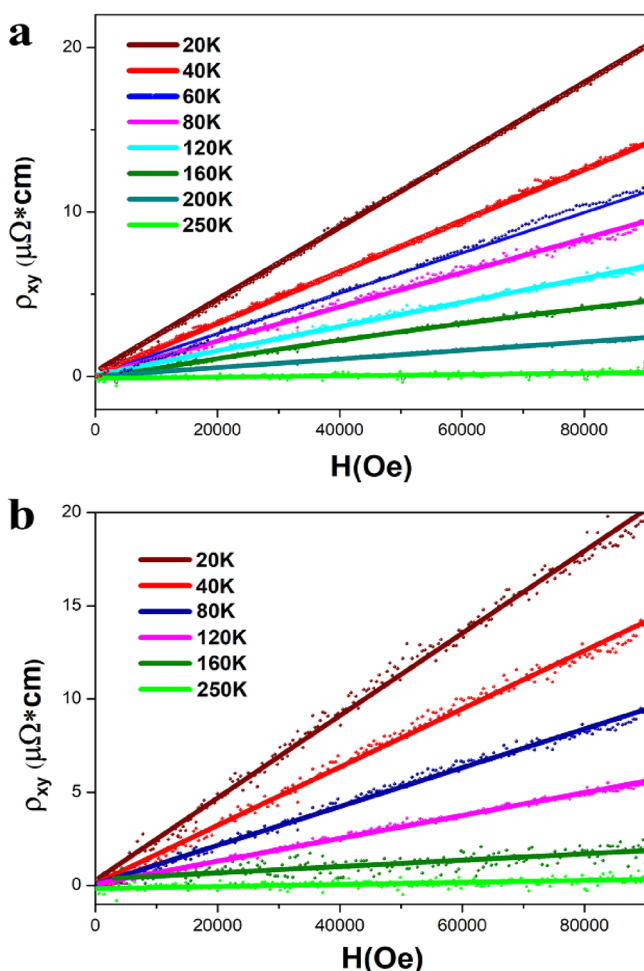


**Figure 6.** (a, b) Field dependence of Hall transverse resistivity  $\rho_{xy}$  for  $S_{0.24}(\text{NH}_3)_{0.26}\text{Fe}_2\text{Se}_2$  and  $\text{Se}_{0.24}(\text{NH}_3)_{0.21}\text{Fe}_2\text{Se}_2$ .

**Structural Characterization and Composition Determination.** Neutron powder diffraction (NPD) experiments were conducted using Ge 311 ( $\lambda = 2.0775 \text{ \AA}$ ) monochromators. Data were collected over the  $2\theta$  ranges  $3.0\text{--}160.0^\circ$  (Ge 311) with a step size of  $0.05^\circ$  at 295 K. The NPD experiments were carried out in the NIST Center for Neutron Research. Powder X-ray diffraction (PXRD) patterns were collected at room-temperature on a PANalytical X'pert Pro X-ray diffractometer operated at 40 kV voltage and 40 mA current using Cu K $\alpha$  radiation ( $\lambda = 1.5406 \text{ \AA}$ ). The  $2\theta$  range was  $10\text{--}80^\circ$  with a step size of 0.02. Indexing and Rietveld refinement were performed using the DICVOL91 and FULLPROF programs. Single crystal X-ray diffraction (SCXRD) patterns at 295 K were collected using a Bruker D8 VENTURE PHOTO II diffractometer with multilayer mirror monochromatized Mo K $\alpha$  ( $\lambda = 0.71073 \text{ \AA}$ ) radiation. Unit cell refinement and data merging were performed using the SAINT program, and an absorption correction was applied using Multi-Scans scanning. Structural solutions with the  $I4/mmm$  space groups were obtained for  $S_{0.12}(\text{NH}_3)_{0.26}\text{Fe}_2\text{Se}_2$  and  $\text{Se}_{0.24}(\text{NH}_3)_{0.21}\text{Fe}_2\text{Se}_2$  by intrinsic phasing methods using the program Superflip, and the final refinement was completed with the Jana2006 suite of programs. The Fe occupancy is refined during the final cycles of refinements against single crystal and neutron powder diffraction data, and no obvious vacancy is evident. We hence fixed the Fe and Se site to be stoichiometric at the end of the refinements. The electron density maps of the two samples were first constructed by charge flipping method implemented in the Jana2006 software. Scanning electron microscopy (SEM) images (Figure S1) were taken on a Phenom pro XL microscope equipped with an electron microprobe analyzer for the semiquantitative elemental analysis in the energy

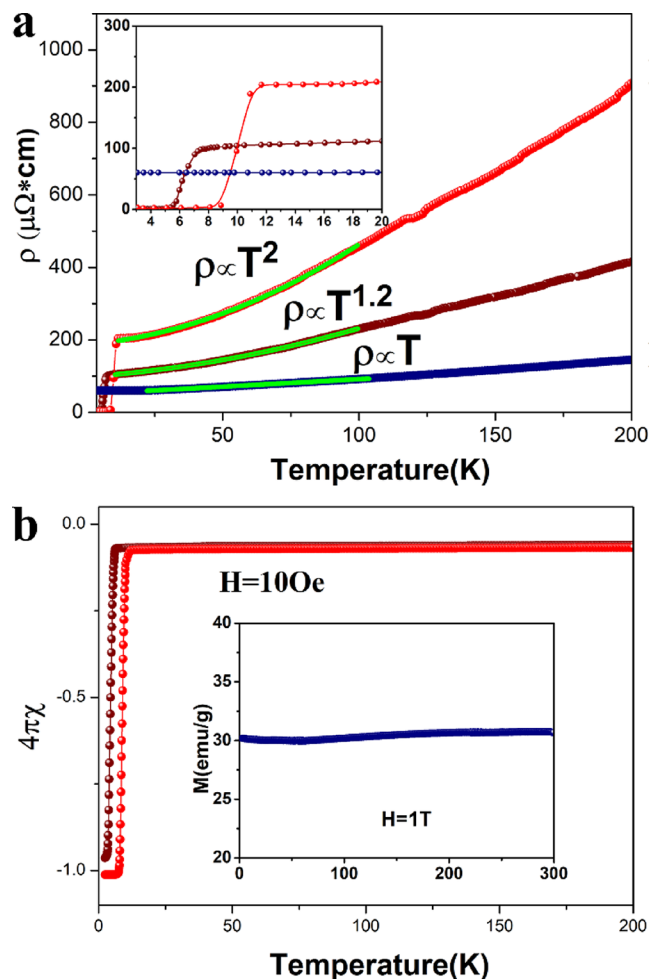


**Figure 7.** (a) Temperature dependence of the electric resistivity  $\rho$  of  $S_{0.12}(\text{NH}_3)_{0.26}\text{Fe}_2\text{Se}_2$  (wine),  $S_{0.24}(\text{NH}_3)_{0.26}\text{Fe}_2\text{Se}_2$  (red), and  $\text{Se}_{0.24}(\text{NH}_3)_{0.21}\text{Fe}_2\text{Se}_2$  (blue). The data are fitted based on the power-law form  $\rho = \rho_0 + AT^n$ . Inset: expanded view around  $T_c$ . (b) Zero-field cooled (ZFC) magnetization for  $S_{0.12}(\text{NH}_3)_{0.26}\text{Fe}_2\text{Se}_2$  (wine) and  $S_{0.24}(\text{NH}_3)_{0.26}\text{Fe}_2\text{Se}_2$  (red) ( $H_{dc} = 10 \text{ Oe}$ ), and the inset is the ZFC magnetization for  $\text{Se}_{0.24}(\text{NH}_3)_{0.21}\text{Fe}_2\text{Se}_2$  ( $H = 1 \text{ T}$ ).

dispersive X-ray spectroscopy (EDX) mode. CHN elemental analysis was performed on a CE-440 CHN elemental analyzer to determine the type of intercalated molecules. Thermogravimetric analyses (TGA) were carried out to confirm the content of  $\text{NH}_3$  molecule using a Q600SDT thermal analyzer under  $\text{N}_2$  atmosphere in the temperature range of  $30\text{--}450^\circ\text{C}$ . The outcomes of the chemistry analyses are listed in Tables S2–S4. X-ray photoelectron spectroscopy (XPS) data were collected with a PHI Versa Probe Scanning XPS Microprobe using Al(K $\alpha$ ) radiation (1486 eV). Ribbons were transferred to a carbon substrate for XPS measurement.  $^{57}\text{Fe}$  Mössbauer spectra were recorded using a constant-acceleration spectrometer, a helium bath cryostat and a  $^{57}\text{Co}(\text{Rh})$  Mössbauer point source with an active spot diameter of 0.5 mm. Isomer shift values are quoted relative to  $\alpha\text{-Fe}$  at 293 K. The high-angle annular-dark-field (HAADF) images were obtained using an ARM-200F (JEOL, Tokyo, Japan) scanning transmission electron microscope (STEM) operated at 200 kV with a CEOS Cs corrector (CEOS GmbH, Heidelberg, Germany) to cope with the probe forming objective spherical aberration.

**Magnetic Susceptibility and Resistivity.** Magnetization and resistivity measurements were carried out using a SQUID PPMS-9 system (Quantum Design). Magnetic susceptibility measurements were made in dc fields of 10 Oe in the temperature range 5–300 K

after cooling in zero applied field (ZFC). Temperature dependence of the resistivity  $\rho(T)$  of  $\text{Se}/\text{S}_x(\text{NH}_3)_y\text{Fe}_2\text{Se}_2$  was measured in a standard four-probe configuration with the applied current less than 2 mA. The Hall coefficients ( $R_H$ ) of  $\text{Se}/\text{S}_x(\text{NH}_3)_y\text{Fe}_2\text{Se}_2$  were obtained by a linear fit of Hall resistivity ( $\rho_{xy}$ ) and B from  $-9$  to  $+9$  T at the temperatures 20, 40, 60, 80, 120, 160, 200, and 250 K, respectively.

**Theoretical Calculations.** Theoretically derived electron densities of  $\text{Se}/\text{S}_x(\text{NH}_3)_y\text{Fe}_2\text{Se}_2$  were obtained from periodic ab initio DFT calculations based on the experimental geometry using the WIEN2k program package. The experimentally determined crystal structures including the internal atomic positions were used for calculations, the charge neutral  $\text{NH}_3$  molecular is omitted for simplicity. Calculations were performed using the Perdew–Burke–Ernzerhof functional on 10000 k grids used for sampling the first Brillouin zone. The required mesh for the calculation planes was obtained with Xcrysden software. Bader analysis based on the theoretically derived electron densities were performed with AIM packages in WIEN2K. DFT calculations were carried out using the linearized augmented plane wave method as implemented in WIEN2k to theoretically study the band structures for  $\text{S}_{0.24}(\text{NH}_3)_{0.26}\text{Fe}_2\text{Se}_2$ ,  $\text{Se}_{0.24}(\text{NH}_3)_{0.21}\text{Fe}_2\text{Se}_2$ , and  $\text{FeSe}$  (Figure S6). To account for correlation effects, we used fully charge self-consistent dynamical mean field theory combined with density functional theory (DFT+DMFT) to calculate the electronic structures shown in Figure 5. Inverse temperature is set to be  $1/116 \text{ K}^{-1}$  to ensure the tetragonal phase of  $\text{FeSe}$  is stable, and the electronic structure of the three compounds can be directly compared. The calculations related to DFT were performed using the local density approximation (LDA). Instead of constructing correlated orbitals from Wannier functions, we used the projection and imbedding process as detailed in ref 40.<sup>41</sup> The impurity problem in DFT+DMFT calculations was solved using the continuous time quantum Monte Carlo (CTQMC) method. The double-counting scheme used in our calculations is the form  $E_{\text{DC}} = U(n_d - 0.5) - J(n_d - 1)/2$ , where  $n_d$  is the Fe 3d occupation and is obtained from self-consistent DFT+DMFT calculations. The value of the on-site Coulomb repulsion ( $U$ ) is 5.0, and the Hund's coupling is 0.8.<sup>42,43</sup>

## ■ ASSOCIATED CONTENT

### Supporting Information

The Supporting Information is available free of charge on the ACS Publications website at DOI: 10.1021/jacs.9b05899.

X-ray data for  $\text{S}_{0.12}\text{Fe}_2\text{Se}_2$  (CIF)

X-ray data for  $\text{Se}_{0.24}\text{Fe}_2\text{Se}_2$  (CIF)

Supplementary figures and tables, including crystallographic data (PDF)

## ■ AUTHOR INFORMATION

### Corresponding Authors

\*shifengjin@iphy.ac.cn

\*chenx29@iphy.ac.cn

### ORCID

Shifeng Jin: 0000-0001-5209-5257

Lin Gu: 0000-0002-7504-031X

Xiaolong Chen: 0000-0001-8455-2117

### Notes

The authors declare no competing financial interest.

Crystallographic data (deposition nos. 1911470–1911471) are provided free of charge by the joint Cambridge Crystallographic Data Centre and Fachinformationszentrum Karlsruhe Access Structures service at [www.ccdc.cam.ac.uk/structures](http://www.ccdc.cam.ac.uk/structures).

## ■ ACKNOWLEDGMENTS

This work is financially supported by the National Key Research and Development of China (2016YFA0300301,

2018YFE0202600), the National Natural Science Foundation of China (Grant Nos. 51772323, 51532010, 91422303, and 51832010), and the Key Research Program of Frontier Sciences, CAS (Grant No. QYZDJ-SSW-SLH013). S.J. is grateful for the support from the Youth Innovation Promotion Association of CAS (2019005).

## ■ REFERENCES

- (1) Warmuth, W. M.; Schollhorn, R., Eds. *Progress in Intercalation Research*; Kluwer: Dordrecht, The Netherlands, 1994.
- (2) Kang, K.; Meng, Y. S.; Breger, J.; Grey, C. P.; Ceder, G. Electrodes with High Power and High Capacity for Rechargeable Lithium Batteries. *Science* **2006**, *311*, 977.
- (3) Mizushima, K.; Jones, P. C.; Wiseman, P. G.; Goodenough, J. B.  $\text{Li}_x\text{CoO}_2$  ( $0 < x < 1$ ):  $\text{S}_{0.12}\text{Fe}_2\text{Se}_2$  A NEW CATHODE MATERIAL FOR BATTERIES OF HIGH ENERGY DENSITY. *Mater. Res. Bull.* **1980**, *15*, 783.
- (4) Tarascon, J. M.; Armand, M. Building better batteries. *Nature* **2008**, *451*, 652.
- (5) DeLongchamp, D. M.; Hammond, P. T. Multiple-Color Electrochromism from Layer-by-Layer-Assembled Polyaniline/ Prussian Blue Nanocomposite Thin Films. *Chem. Mater.* **2004**, *16* (23), 4799–4805.
- (6) Halim, J.; Lukatskaya, M. R.; Cook, K. M.; Lu, J.; Smith, C. R.; Näslund, L.; May, S. J.; Hultman, L.; Gogotsi, Y.; Eklund, P.; Barsoum, M. W. Transparent Conductive Two-Dimensional Titanium Carbide Epitaxial Thin Films. *Chem. Mater.* **2014**, *26* (7), 2374–2381.
- (7) Wray, L. A.; Xu, S. Y.; Xia, Y.; Hor, Y. S.; Qian, D.; Fedrov, A.; Lin, H.; Bansil, A.; Cava, R. J.; Hasan, M. Z. A topological insulator under strong Coulomb, magnetic and disorder perturbations. *Nat. Phys.* **2010**, *6*, 855.
- (8) Jacobson, A. J.; Nazar, L. F. Intercalation Chemistry. *Encyclopedia of Inorganic and Bioinorganic Chemistry*; John Wiley & Sons, Ltd., 2011.
- (9) Khan, A. I.; O'Hare, D. Intercalation chemistry of layered double hydroxides: recent developments and applications. *J. Mater. Chem.* **2002**, *12*, 3191.
- (10) Shen, C.; Mayorga, S. G.; Biagioni, R.; Piskoti, C.; Ishigami, M.; Zettl, A.; Bartlett, N. Intercalation of Hexagonal Boron Nitride by Strong Oxidizers and Evidence for the Metallic Nature of the Products. *J. Solid State Chem.* **1999**, *147*, 74–81.
- (11) Hsu, F. C.; Luo, J. Y.; Yeh, K. W.; Chen, T. K.; Huang, T. W.; Wu, P. M.; Lee, Y. C.; Huang, Y. L.; Chu, Y. Y.; Yan, D. C.; Wu, M. K. Superconductivity in PbO-type Structure  $\text{FeSe}$ . *Proc. Natl. Acad. Sci. U. S. A.* **2008**, *105*, 14262.
- (12) Yamanaka, S. Intercalation and superconductivity in ternary layer structured metal nitride halides ( $\text{MNX}$ :  $M = \text{Ti, Zr, Hf}$ ;  $X = \text{Cl, Br, I}$ ). *J. Mater. Chem.* **2010**, *20*, 2922–2933.
- (13) Kargina, I.; Richeson, D. Diamine Intercalates of Titanium and Vanadium Oxychloride. Evidence for the Subsequent Substitution Reactions of  $\text{TiOCl}$  with Amines. *Chem. Mater.* **1996**, *8* (2), 480–485.
- (14) Mathey, Y.; Clement, R.; Sourisseau, C.; Lucazeau, G. Vibrational study of layered  $\text{MPX}_3$  compounds and of some intercalates with  $\text{Co}(\text{eta}^5\text{-C}_5\text{H}_5)^{2+}$  or  $\text{Cr}(\text{eta}^6\text{-C}_6\text{H}_6)^{2+}$ . *Inorg. Chem.* **1980**, *19*, 2773.
- (15) Levy, F., Ed. *Intercalated Layered Materials*; Reidel: Dordrecht, The Netherlands, 1979.
- (16) McQueen, T. M.; Williams, A. J.; Stephens, P. W.; Tao, J.; Zhu, Y.; Ksenofontov, V.; Casper, F.; Felser, C.; Cava, R. J. Tetragonal-to-Orthorhombic Structural Phase Transition at 90 K in the Superconductor  $\text{Fe}_{1.01}\text{Se}$ . *Phys. Rev. Lett.* **2009**, *103*, No. 057002.
- (17) Urata, T.; Tanabe, Y.; Huynh, K. K.; Yamakawa, Y.; Kontani, H.; Tanigaki, K. Argument on superconductivity pairing mechanism from cobalt impurity doping in  $\text{FeSe}$ : spin ( $s_{\pm}$ ) or orbital ( $s_{++}$ ) fluctuation. *Phys. Rev. B: Condens. Matter Mater. Phys.* **2016**, *93*, No. 014507.

- (18) Dagotto, E. *Colloquium: The unexpected properties of alkali metal iron selenide superconductors*. *Rev. Mod. Phys.* **2013**, *85*, 849–867.
- (19) Guo, J. G.; Jin, S. F.; Wang, G.; Wang, S. C.; Zhu, K. X.; Zhou, T. T.; He, M.; Chen, X. L. Superconductivity in the iron selenide  $K_x\text{Fe}_2\text{Se}_2$  ( $0 \leq x \leq 1.0$ ). *Phys. Rev. B: Condens. Matter Mater. Phys.* **2010**, *82*, 180520.
- (20) Burrard-Lucas, M.; Free, D. G.; Sedlmaier, S. J.; Wright, J. D.; Cassidy, S. J.; Hara, Y.; Corkett, A. J.; Lancaster, T.; Baker, P. J.; Blundell, S. J.; Clarke, S. J. Enhancement of the superconducting transition temperature of FeSe by intercalation of a molecular spacer layer. *Nat. Mater.* **2013**, *12*, 3464.
- (21) Guo, J.; Lei, H.; Hayashi, F.; Hosono, H. Superconductivity and phase instability of  $\text{NH}_3$ -free Na-intercalated  $\text{FeSe}_{1-z}\text{Sz}$ . *Nat. Commun.* **2014**, *5*, 4756.
- (22) Ying, T. P.; Chen, X. L.; Wang, G.; Jin, S. F.; Zhou, T. T.; Lai, X. F.; Zhang, H.; Wang, W. Y. Observation of superconductivity at 3046K in  $\text{A}_x\text{Fe}_2\text{Se}_2$  (A = Li, Na, Ba, Sr, Ca, Yb, and Eu). *Sci. Rep.* **2012**, *2*, 426.
- (23) Ying, T. P.; Chen, X. L.; Wang, G.; Jin, S. F.; Lai, X. F.; Zhou, T. T.; Zhang, H.; Shen, S. J.; Wang, W. Y. Superconducting phases in potassium-intercalated iron selenides. *J. Am. Chem. Soc.* **2013**, *135*, 2951–2954.
- (24) Shi, M. Z.; Wang, N. Z.; Lei, B.; Shang, C.; Meng, F. B.; Ma, L. K.; Zhang, F. X.; Kuang, D. Z.; Chen, X. H. Organic-ion-intercalated FeSe-based superconductors. *Phys. Rev. Materials* **2018**, *2*, No. 074801.
- (25) Lu, X. F.; Wang, N. Z.; Wu, H.; Wu, Y. P.; Zhao, D.; Zeng, X. Z.; Luo, X. G.; Wu, T.; Bao, W.; Zhang, G. H.; Huang, F. Q.; Huang, Q. Z.; Chen, X. H. Coexistence of superconductivity and antiferromagnetism in  $(\text{Li}_{0.8}\text{Fe}_{0.2})\text{OHFeSe}$ . *Nat. Mater.* **2015**, *15*, 4155.
- (26) Sun, R. J.; Quan, Y.; Jin, S. F.; Huang, Q. Z.; Wu, H.; Zhao, L.; Gu, L.; Yin, Z. P.; Chen, X. L. Realization of continuous electron doping in bulk iron selenides and identification of a new superconducting zone. *Phys. Rev. B: Condens. Matter Mater. Phys.* **2018**, *98*, 214508.
- (27) Jin, S.; Fan, X.; Wu, X.; Sun, R.; Wu, H.; Huang, Q.; Shi, C.; Xi, X.; Li, Z.; Chen, X. High  $T_C$  Superconducting phases in Organic Molecular Intercalated Iron Selenides: Synthesis and Crystal Structures. *Chem. Commun.* **2017**, *53*, 9729–9732.
- (28) Mou, D.; Liu, S.; Jia, X.; He, J.; Peng, Y.; Zhao, L.; Yu, L.; Liu, G.; He, S.; Dong, X.; Zhang, J.; Wang, H.; Dong, C.; Fang, M.; Wang, X.; Peng, Q.; Wang, Z.; Zhang, S.; Yang, F.; Xu, Z.; Chen, C.; Zhou, X. J. Distinct Fermi Surface Topology and Nodeless Superconducting Gap in a  $(\text{Tl}_{0.58}\text{Rb}_{0.42})\text{Fe}_{1.72}\text{Se}_2$  Superconductor. *Phys. Rev. Lett.* **2011**, *106*, 107001.
- (29) Zhang, P.; Yaji, K.; Hashimoto, T.; Ota, Y.; Kondo, T.; Okazaki, K.; Wang, Z.; Wen, J.; Gu, G. D.; Ding, H.; Shin, S. Observation of topological superconductivity on the surface of an iron-based superconductor. *Science* **2018**, *360*, 182–186.
- (30) Petricek, V.; Dusek, M.; Palatinus, L. Z. Crystallographic Computing System JANA2006: General features. *Z. Kristallogr. - Cryst. Mater.* **2014**, *229* (5), 345–352.
- (31) Shenasa, M.; Sainkar, S.; Lichtman, D. XPS study of some selected selenium compounds. *J. Electron Spectrosc. Relat. Phenom.* **1986**, *40*, 329.
- (32) Kim, Y. I.; Hatfield, W. E. Electrical, magnetic and spectroscopic properties of tetrathiafulvalene charge transfer compounds with iron, ruthenium, rhodium and iridium halides. *Inorg. Chim. Acta* **1991**, *188*, 15.
- (33) Tkachenko, O. P.; Shpiro, E. S.; Wark, M.; Schulz-Ekloff, G.; Jaeger, N. I. X-ray photoelectron/X-ray excited auger electron spectroscopic study of highly dispersed semiconductor CdS and CdO species in zeolites. *J. Chem. Soc., Faraday Trans.* **1993**, *89*, 3987.
- (34) Shul'ga, Y. M.; Rubtsov, V. I.; Vasilets, V. N.; Lobach, A. S.; Spitsyna, N. G.; Yagubskii, E. B. EELS, XPS and IR study of  $\text{C}_{60}\text{2S}_8$  compound. *Synth. Met.* **1995**, *70*, 1381.
- (35) Binder, H.; Sellmann, D. X-ray Photoelectron Studies of Pentacarbonyl Chromium and Tungsten Complexes with Nitrogen Ligands. *Z. Naturforsch., B: J. Chem. Sci.* **1978**, *33*, 173.
- (36) Kocher, N.; Henn, J.; Gostevskii, B.; Kost, D.; Kalikhman, I.; Engels, B.; Stalke, D. Si-E (E) N, O, F) Bonding in a Hexacoordinated Silicon Complex: New Facts from Experimental and Theoretical Charge Density Studies. *J. Am. Chem. Soc.* **2004**, *126*, 5563–5568.
- (37) Pillet, S.; Wu, G.; Kulsomphob, V.; Harvey, B. G.; Ernst, R. D.; Coppens, P. Investigation of Zr-C, Zr-N, and Potential Agostic Interactions in an Organozirconium Complex by Experimental Electron Density Analysis. *J. Am. Chem. Soc.* **2003**, *125* (7), 1937–1949.
- (38) Subedi, A.; Zhang, L.; Singh, D. J.; Du, M. H. Density functional study of FeS, FeSe, and FeTe: Electronic structure, magnetism, phonons, and superconductivity. *Phys. Rev. B: Condens. Matter Mater. Phys.* **2008**, *78*, 134514.
- (39) Nakayama, K.; Miyata, Y.; Phan, G. N.; Sato, T.; Tanabe, Y.; Urata, T.; Tanigaki, K.; Takahashi, T. Reconstruction of band structure induced by electronic nematicity in an FeSe superconductor. *Phys. Rev. Lett.* **2014**, *113*, 237001.
- (40) Cheng, B.; Chen, Z. G.; Zhang, C. L.; Ruan, R. H.; Dong, T.; Hu, B. F.; Guo, W. T.; Miao, S. S.; Zheng, P.; Luo, J. L.; Xu, G.; Dai, P.; Wang, N. L. Three-dimensionality of band structure and a large residual quasiparticle population in  $\text{Ba}_{0.67}\text{K}_{0.33}\text{Fe}_2\text{As}_2$  as revealed by c-axis polarized optical measurements. *Phys. Rev. B: Condens. Matter Mater. Phys.* **2011**, *83*, 144522.
- (41) Haule, K.; Yee, C.; Kim, K. Dynamical mean-field theory within the full-potential methods: Electronic structure of  $\text{CeIrIn}_5$ ,  $\text{CeCoIn}_5$ , and  $\text{CeRhIn}_5$ . *Phys. Rev. B: Condens. Matter Mater. Phys.* **2010**, *81*, 195107.
- (42) Blaha, P. *WIEN2K, An Augmented Plane Wave + Local Orbitals Program for Calculating Crystal Properties*, 2001.
- (43) Kotliar, G. Electronic structure calculations with dynamical mean-field theory. *Rev. Mod. Phys.* **2006**, *78*, 865.